Available online at www.sciencedirect.com
SCIENCE DIRECT®
Advances in Water Resources 26 (2003) 733–746
Advances in Water Resources
www.elsevier.com/locate/advwatres

Numerical validation of the land surface process component of an LSP/R model

Jasmeet Judge [a,*], Linda M. Abriola [b], Anthony W. England [c]

[a] Center for Remote Sensing, Agricultural and Biological Engineering Department, Institute of Food and Agricultural Sciences, The University of Florida, P.O. Box 110570, Gainesville, FL 32611, USA
[b] Department of Civil and Environmental Engineering, The University of Michigan, 1315 GG Brown, 1301 Beal Ave., Ann Arbor, MI 48109, USA
[c] Department of Electrical Engineering and Computer Science and Department of Atmospheric, Oceanic, and Space Sciences, The University of Michigan, 3240 EECS Bldg., 1301 Beal Ave., Ann Arbor, MI 48109, USA

Received 23 July 2002; received in revised form 24 March 2003; accepted 2 April 2003

Abstract

The University of Michigan's land surface process/radiobrightness (LSP/R) model was developed as a step toward linking a traditional SVAT model to satellite microwave observations. The LSP model simulates land–air interactions and estimates surface fluxes, temperature and moisture profiles in soil and vegetation when forced with observed weather. These estimates are used by a microwave emission model, called the R model, that predicts terrain brightness temperatures. In this paper, we evaluate accuracy of the numerical methods used in the LSP model. Such rigorous tests were not conducted during the early development of the model. We describe three test-scenarios that included comparing the numerical solution with an analytic solution, evaluating coupled energy and moisture transport for a simple case, and calculating errors in energy and mass balance in the model for a realistic case using field observations. The original version of the model was modified to make it more applicable to the field conditions for the third test-case. Results from these tests demonstrate the physical self-consistency of the model and its successful implementation for the simple scenarios, and argue for its extendibility to more realistically complex cases.

1. Introduction

Soil vegetation atmosphere transfer (SVAT) models are used to simulate energy, moisture, and momentum fluxes at the lower boundary of atmospheric general circulation models (AGCMs). Examples of SVAT models include biosphere atmosphere transfer scheme (BATS) [9,10], simple biosphere-2 (SiB-2) model [45], simple SiB (SSiB) [49], land surface model (LSM) [2], and variable infiltration capacity (VIC) model [28,29]. A functional requirement of these models is that they maintain estimates of the stored water field, i.e., estimates of the spatial distribution of water stored in soil, snow, and vegetation that is available to the atmosphere through evaporation and transpiration. It is well known that the AGCMs' predictions for continental weather and near-term climate are highly sensitive to errors in these stored water estimates [1].

Microwave brightness at longer wavelengths, for example at 20 cm, is usefully sensitive to near-surface soil moisture and temperature profiles through most vegetation canopies [20,21,44]. This sensitivity to near-surface moisture enables a satellite technique for reliably inferring the stored water field. While the microwave brightness is sensitive to moisture only in the upper few centimeters of soil, assimilation of near-daily observations using an appropriate SVAT model can yield soil moisture profiles to depths of a meter or more [3,11,13,19,27,41,42,48]. For such assimilation to result in convergence to an accurate moisture profile, there cannot be systematic errors in the SVAT thermal or moisture transport processes, or in the radiobrightness (R) relationship to near-surface soil moisture distribution. Our current knowledge of the underlying physics permits highly accurate model simulations of thermal and moisture transport processes in unsaturated soils [4,34], even though the computational demands of AGCMs have required extensive simplifying parameterizations of conventional SVAT models [46].

* Corresponding author.
E-mail address: jasmeet@agen.ufl.edu (J. Judge).

0309-1708/03/$ - see front matter © 2003 Elsevier Science Ltd. All rights reserved.
doi:10.1016/S0309-1708(03)00048-4

The University of Michigan's Microwave Geophysics Group (UM-MGG) has developed a series of terrain-specific physically based SVAT models that are linked to microwave emission models [12,24,31–33]. Unlike most SVAT models intended for use with AGCMs, the Michigan's land surface process (LSP) models are diagnostic models in that they strive for physical fidelity at the cost of computational complexity. They simulate one-dimensional coupled heat and moisture transport in unsaturated soils [7,39] when forced with observed downwelling short and long-wave radiation, and micrometeorological observations of air temperature, relative humidity, wind speed, and precipitation. They are initialized with observed soil temperature and moisture profiles augmented at depths below 1 m with model-based climatic profiles. Estimates of soil and canopy moisture and temperatures from the LSP models are used by the microwave emission or R models to predict brightness temperatures (see Fig. 1). As our models evolved, we sought more rigorous means for testing their integrity. In this paper, we present a numerical validation of the LSP model developed by Liou and England [33] for prairie grasslands. We demonstrate its internal consistency and its agreement with an analytical solution for a simplified system. We also extend the model to a realistic complex system and check errors in energy and moisture balance.

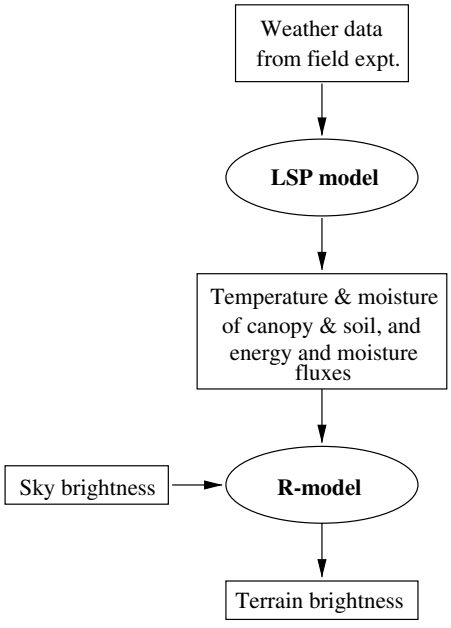

Fig. 1. A flow diagram of interactions between the LSP and R models in the LSP/R model.

2. The LSP model for prairie grasslands

2.1. Biophysics and governing equations

The LSP model (called 1-dH module in the original model) consists of bi-layered vegetation over a soil whose constitutive properties are constant throughout the profile. Fig. 2 shows the land surface processes simulated in the model. Vegetation cover can be assigned from 0% (bare soil) to 100% (continuous canopy). The vegetation includes a photosynthetically active canopy layer and a thermally insulating, non-photosynthetic thatch layer. The thatch is very simplistic in the model with no moisture holding capacity, does not affect the moisture exchanges between the canopy and the soil, but does influence the exchange of radiant energy between the soil and the photosynthetically active layer.

The soil is divided into 60 computational blocks. Because soil closer to the surface is more influenced by rapid changes in weather and downwelling radiance, thicknesses of the blocks increase exponentially with depth. When vegetation is present, the upper blocks also serve as a root-zone where moisture for transpiration is drawn from the soil, as shown in Fig. 2. The constitutive properties of soil, such as moisture and thermal diffusivities, tortuosity, thermal conductivity, and water retention, are estimated from empirical models that have earned acceptance in the literature [8,25,26,31,43]. The moisture and energy balance equations for the soil are [7,39]:

$$\frac{\partial X_{\mathrm{m}}}{\partial t} = -\nabla \cdot \vec{q}_{\mathrm{m}} \quad \frac{\partial X_{\mathrm{h}}}{\partial t} = -\nabla \cdot \vec{q}_{\mathrm{h}} \tag{1a}$$

$$\begin{aligned} X_{\mathrm{m}} &= \rho_{\mathrm{l}}(\theta_{\mathrm{l}} + \theta_{\mathrm{v}}) \\ X_{\mathrm{h}} &= C_{\mathrm{m}}(T - T_0) + L_0\rho_{\mathrm{l}}\theta_{\mathrm{v}} + \rho_{\mathrm{l}}\int_0^{\theta_{\mathrm{l}}} W\,\mathrm{d}\theta \end{aligned} \tag{1b}$$

$$\begin{aligned} \vec{q}_{\mathrm{m}} &= -\rho_{\mathrm{l}}(D_T\nabla T + D_\theta\nabla\theta + K\hat{\boldsymbol{k}}) \\ \vec{q}_{\mathrm{h}} &= -\lambda\nabla T + L_0\vec{q}_{\mathrm{v}} + (c_p q_{\mathrm{v}} + c_{\mathrm{l}} q_{\mathrm{l}})(T - T_0) \end{aligned} \tag{1c}$$

where, all the symbols above are defined in Appendix A.

The energy fluxes in the canopy layer are primarily driven by insolation and canopy thermal infrared (TIR) emission, while moisture fluxes are driven by evaporation and transpiration. The energy and moisture transport equations for the canopy are:

$$\frac{\partial X_{\mathrm{mc}}}{\partial t} = \rho_{\mathrm{l}}(P_{\mathrm{c}} - D_{\mathrm{c}} - E_{\mathrm{c}}) \tag{2a}$$

$$\frac{\partial X_{\mathrm{hc}}}{\partial t} = -(H_{\mathrm{c}} + L_{\mathrm{c}} - R_{\mathrm{nc}}) \tag{2b}$$

where, X_{mc} and X_{hc} are the total moisture and heat contents per unit area stored in the canopy, respectively, ($\mathrm{kg/m^2}$ and $\mathrm{J/m^2}$); ρ_{l} is the density of liquid water

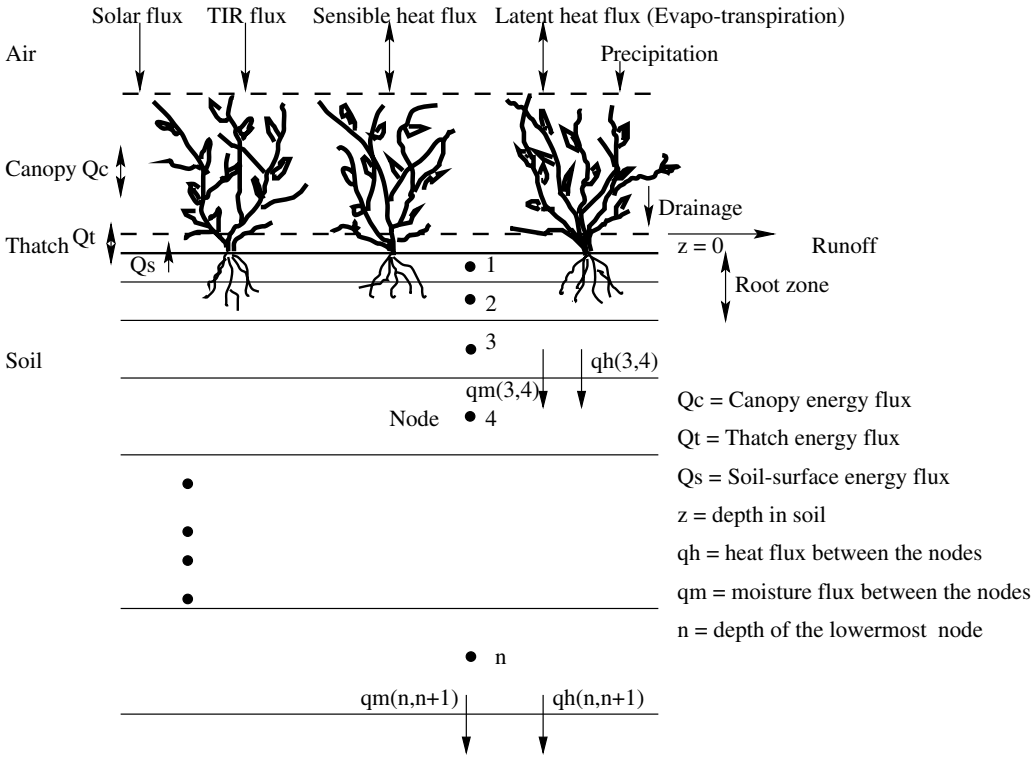

Fig. 2. Land surface processes simulated in the LSP model (adapted from [33]).

(kg/m^3); P_c, D_c and E_c are the rates of precipitation, water drainage and evaporation (m/s); H_c is the sensible heat flux between the atmosphere and the canopy (W/m^2); L_c is the latent heat flux between the atmosphere and the canopy due to evapotranspiration (W/m^2) and R_{nc} is the net radiation (longwave and shortwave) absorbed by the canopy (W/m^2). The suction from root zone affecting the latent heat flux is modeled following Verseghy et al. [47] and Noilhan and Planton [35].

The moisture and energy fluxes across the upper boundary, i.e., at the interface between soil and vegetation, are driven by net precipitation and radiation reaching the soil surface as follows:

$$q_m(0,1) = \rho_l(D_c - E_s - E_{tr} - \text{runoff}) \tag{3a}$$

$$q_h(0,1) = R_{ns} - H - L \tag{3b}$$

where,

- $q_m(0,1)$ and $q_h(0,1)$ are the moisture and heat flux densities at the interface between blocks 0 (vegetation) and 1 (soil surface), respectively,
- H and L are the sensible and latent heat fluxes from the soil, respectively (W/m^2),
- D_c is the rate of drainage from the canopy (m/s), D_c = total precipitation – interception by the canopy,
- E_s is the rate of evaporation from the soil (m/s),
- E_{tr} is rate of transpiration from the root zone (m/s) and,
- R_{ns} is the net radiation (longwave and shortwave) absorbed by the soil (W/m^2).

The energy and moisture fluxes across the lower boundary, i.e., at the interface between the nth and $n+1$th computational blocks, are set equal to the fluxes across the interface between $n-1$th and nth block (see Fig. 2). This allows no change in the moisture and heat content of the nth block.

2.2. Numerical algorithm and implementation

Because the vegetation is treated as a separate layer in the model from a numerical standpoint, we describe the numerical algorithm and the validation tests for bare soil (vegetation cover = 0). The non-linear and coupled equations for conservation of moisture and energy in soil (1a) are linearized and solved using an explicit, forward finite difference method [5,33]. In the model, the dynamic response to non-linearity is lagged in time. Combining the Eqs. (1a)–(1c), we obtain two equations of the form:

$$M\frac{\partial\theta_l}{\partial t} + E\frac{\partial T}{\partial t} = X \quad N\frac{\partial\theta_l}{\partial t} + F\frac{\partial T}{\partial t} = Y \tag{4}$$

where, $X = -\nabla\cdot(\vec{q}_m/\rho_l)$, $Y = -\nabla\cdot\vec{q}_h$, and the coefficients M, N, E, and F are dependent on soil properties and are derived in Appendix A. M and E represent the increase in total moisture content with water content

and temperature of soil, respectively. N and F represent the increase in thermal energy with water content and temperature of soil, respectively. $\partial\theta_l/\partial t$ and $\partial T/\partial t$ represent the temporal changes in moisture content and temperature, respectively. Solving the above equations simultaneously,

$$\frac{\partial\theta_l}{\partial t} = \frac{FX - EY}{MF - EN} \quad \frac{\partial T}{\partial t} = \frac{MY - NX}{MF - EN} \tag{5}$$

Fig. 3 gives a schematic representation of the difference method as implemented in the model. It uses a block-centered grid where the soil parameter values for each computational block are assumed to be located at the center of that block. Fig. 4 gives a flow diagram of the computations in the LSP model. To begin, the soil and the vegetation properties are initialized and the initial energy and moisture fluxes are calculated. The model is forced with weather, and a two-dimensional Newton–Raphson technique is applied in conjunction with a finite difference method to balance energy and moisture fluxes at the soil surface. Fig. 5 gives a detailed description of the Newton–Raphson technique used in the model. The boundary-flux matching process is repeated until a specified convergence criterion is satisfied. The resulting new fluxes are used to estimate the new surface temperature and moisture. Once the surface temperature and moisture are estimated, the difference method is employed to calculate the new fluxes, temperature, and moisture for each soil block.

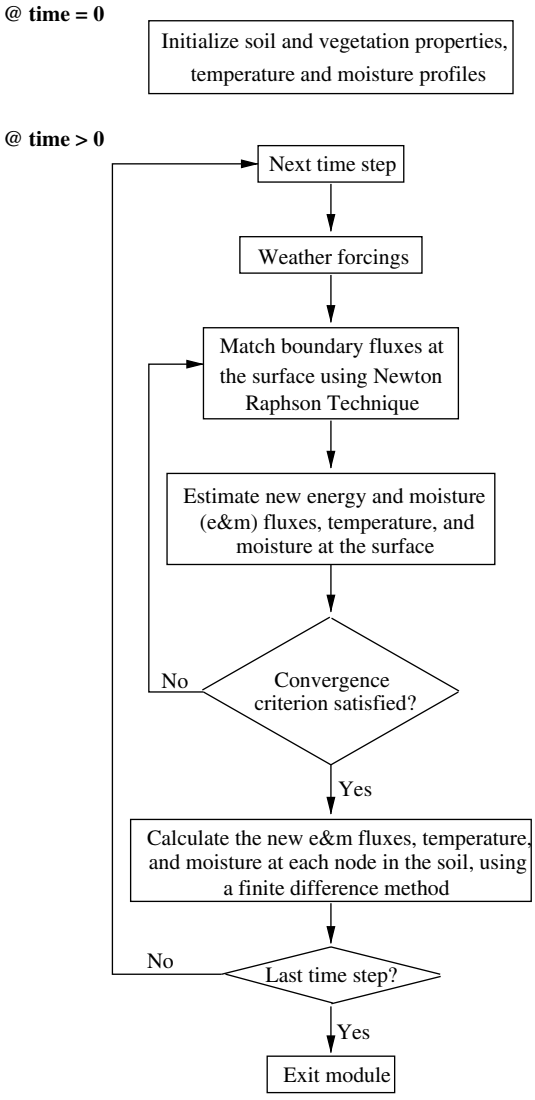

Fig. 4. A flow diagram of LSP model algorithm.

3. Numerical validation

This section describes three tests conducted to ensure that the numerical simulation in the LSP model is implemented correctly, both qualitatively and quantitatively. This validation was critical because such tests were never conducted during the development of the model. As mentioned earlier, all the tests were conducted for bare soil case with vegetation cover set to 0. In the first test, the numerical solution is compared with

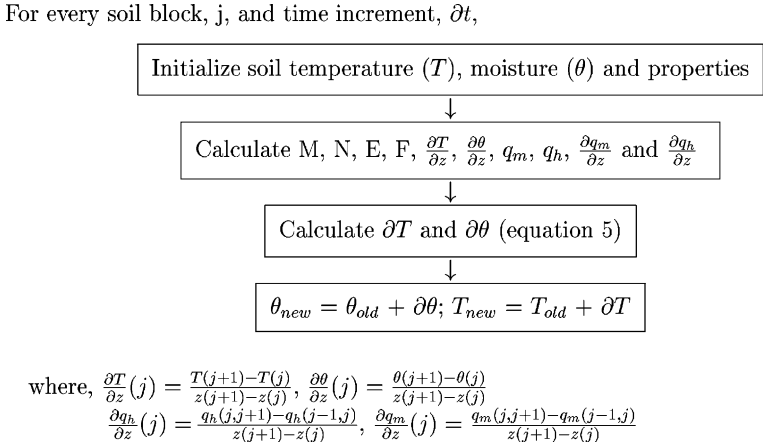

Fig. 3. A schematic representation of the finite difference method used in the LSP model.

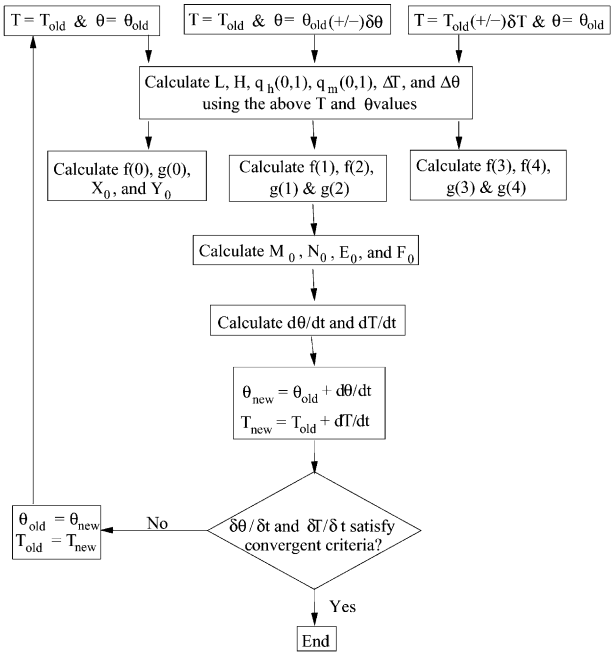

where, $f = M_1\Delta\theta + E_1\Delta T$ $\quad g = N_1\Delta\theta + F_1\Delta T$

$M_0 = \frac{f(2)-f(1)}{2\delta\theta}$ $\quad E_0 = \frac{f(4)-f(3)}{2\delta\theta}$

$N_0 = \frac{g(2)-g(1)}{2\delta T}$ $\quad F_0 = \frac{g(4)-g(3)}{2\delta T}$

$\Delta\theta = \theta - \theta_1$ $\quad \delta\theta = 1\text{x}10^{-10}$

$\Delta T = T - T_1$ $\quad \delta T = 1\text{x}10^{-10}$

L = Latent heat flux $\quad$ H = Sensible heat flux

• Subscripts 0 and 1 refer to the parameter values for the current and the previous time steps, respectively.

Fig. 5. A schematic representation of the computations in the 2-D Newton–Raphson technique in the LSP model.

an analytic solution for a simplified transport problem. In the second test, we confirm that the physics of coupled moisture and energy flow is correctly simulated for a homogeneous soil when a symmetric initial temperature profile is used. In the third, we check errors in mass and energy balance for a realistic simulation using inputs from field observations. We also briefly discuss the modifications made to the model for extending it to the field conditions in the third test case.

3.1. The LSP numerical solution vs. an analytic solution for a simple transport problem

We verify the quantitative accuracy of the model by comparing the finite difference solution with an analytic solution for a simplified problem chosen to model strong coupling between moisture and heat transport in a dry, vapor-dominated system [34]. In this problem, the soil is at an equilibrium temperature (T) and vapor density, (ρ_v) with no heat or moisture flow at the lower boundary. The vapor density is suddenly increased at the upper boundary by ρ_{v0}, while the temperature at the boundary is held constant at T. The vapor diffuses into the soil and releases heat as it condenses. This increases the soil temperatures temporarily, with both the vapor density and the temperatures returning to equilibrium, at their values at the upper boundary [34].

We use an analytic solution for this problem as outlined by Crank [6] and is described in detail in Appendix A. To compare the two solutions, we choose Yolo light clay because it has been extensively studied and its properties (see Table 1) are well documented [18,34,36]. The soil column is 0.1 m thick with the water retention curve given by Eqs. (6a) and (6b). The initial and boundary conditions are given in Eqs. (7a)–(7f). Because the analytic solution is based upon constant soil properties, thermal capacity, latent heat of vaporization, humidity, and thermal conductivity are kept constant in the numerical simulation to achieve a better comparison. The changes in moisture and vapor density with matric potential are also held constant.

$$\theta_m = 0.371\left[1 + \left(\frac{\log(\Psi)}{2.26}\right)^4\right]^{-1} + 0.124 \quad \Psi < 0.01 \text{ m} \tag{6a}$$

Table 1
Soil properties for Yolo light clay and other parameters used to calculate the analytic solution

Properties/parameters	Values
Porosity	0.495
Thermal conductivity	0.165 J/m K s
Thermal capacity	1.673663×10^6 J/m^3 K
Latent heat of vaporization (L)	2.45616×10^6 J/kg
σ_c	0.274 m^3/kg
ω_c	0 K^{-1}
D	3.63×10^{-8} m^2/s
$\mathbb{D}$	9.89×10^{-8} m^2/s
λ_c	0 kg/m^3 K
v_c	395.286 K m^3/kg

The same soil properties were also used by the numerical model.

$$\theta_m = 0.495 \quad \Psi \geqslant 0.01 \text{ m} \tag{6b}$$

$$\rho_v = \rho_v^* \quad t = 0 \quad 0 \leqslant z \leqslant 0.1 \tag{7a}$$

$$T = T^* \quad t = 0 \quad 0 \leqslant z \leqslant 0.1 \tag{7b}$$

$$\rho_v = \rho_v^* + \rho_{v0} \quad t \geqslant 0 \quad z = 0 \tag{7c}$$

$$T = T^* \quad t > 0 \quad z = 0 \tag{7d}$$

$$q_m = 0 \quad t \geqslant 0 \quad z = 0.1 \text{ m} \tag{7e}$$

$$q_h = 0 \quad t \geqslant 0 \quad z = 0.1 \text{ m} \tag{7f}$$

where, Ψ is the matric potential and other symbols are defined in Appendix A.

- $T^* = 293.15$ K and,
- $\rho_v^* = 4.03 \times 10^{-3}$ kg/m^3,
- $\rho_{v0} = 0.63 \times 10^{-3}$ kg/m^3.

Fig. 6(a) and (b) compare the numerical and the analytic solutions for moisture and temperature profiles as time progresses from 10 min to 4 days. The temperature rose as the increased vapor density penetrated into the lower layers and condensed. The system reached equilibrium after ~5 days. The numerical solution follows the analytic solution with a maximum difference of 2.2 mK for temperature and 0.0006% for moisture over the comparison period.

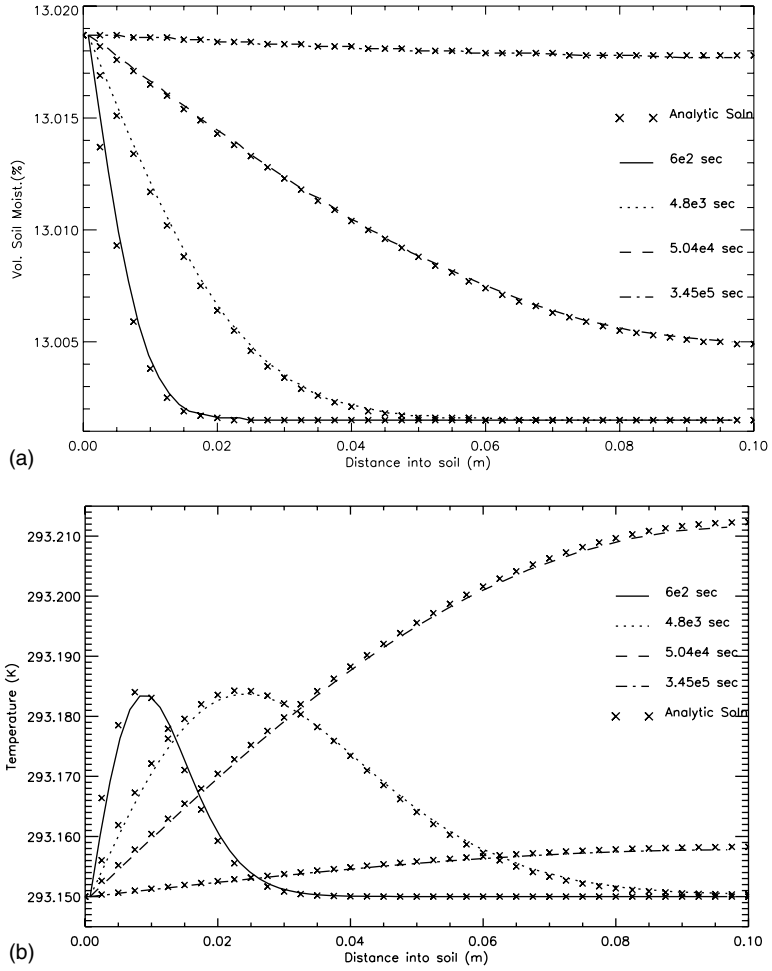

Fig. 6. Comparison of analytic and numerical solution. (a) Volumetric soil moisture profiles. (b) Temperature profiles in soil as functions of time.

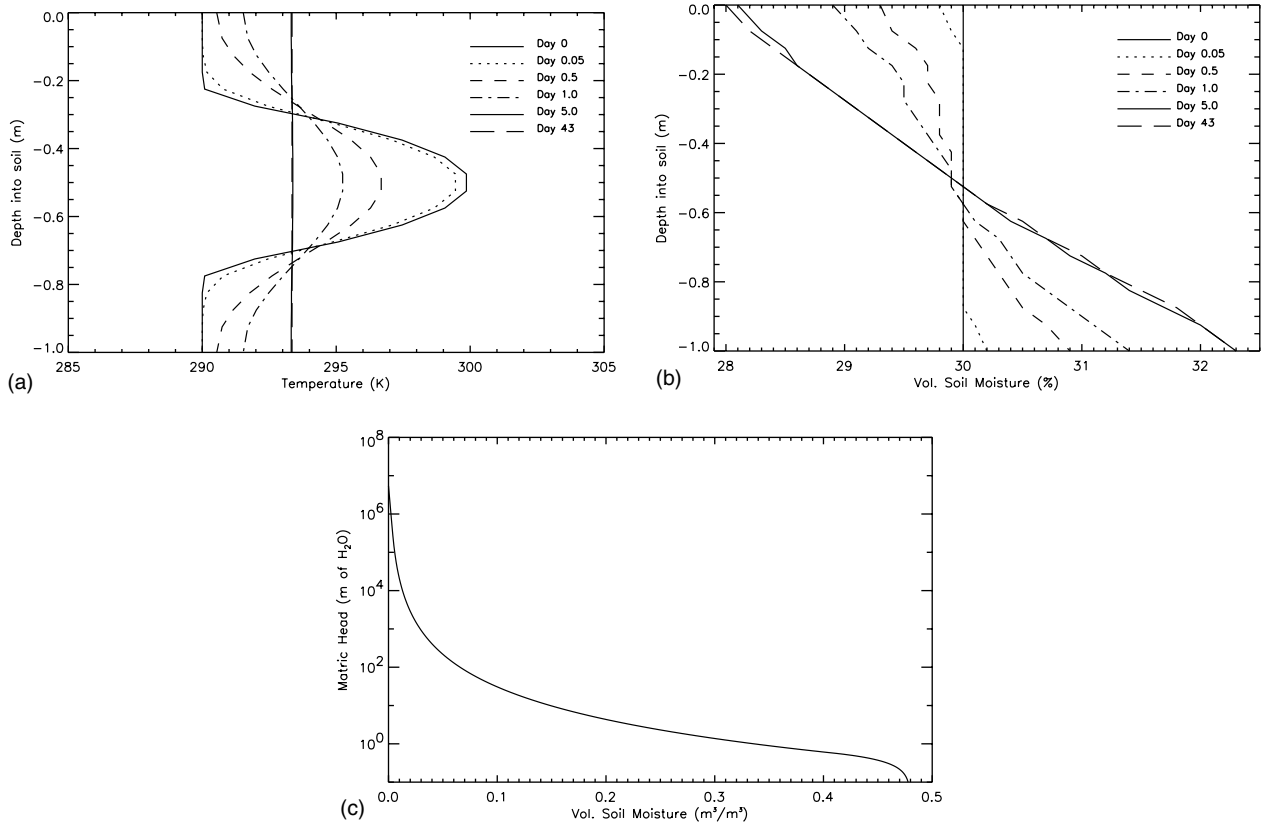

Fig. 7. Propagation of moisture and heat: (a) Temperature profiles and (b) moisture profiles during the 43-day model run. (c) Soil water retention curve from the two-parameter junction model of Rossi and Nimmo [43] at soil temperature 295 K.

3.2. Moisture and energy flow in a homogeneous soil

To confirm the proper implementation of coupled moisture and energy propagation in homogeneous soil profile, the LSP model is run with a symmetric initial temperature profile (Fig. 7(a)), a constant initial moisture profile (0.3 m^3/m^3), and zero heat and moisture fluxes at the upper and lower boundaries. The soil is modeled to a depth of 1 m and discretized into 20 blocks of equal thickness and uniform constitutive properties (see Table 2).

Fig. 7(a) and (b) show the temperature and moisture profiles for selected times during a 43-day model simulation. Heat flows down the temperature gradient, as expected, and the soil achieves equilibrium temperature after ~6 days (Fig. 7(a)). The moisture not only follows the negative of the temperature gradient, but it also follows gravity. Because the capillary retention curve is linear in the vicinity of the moisture value of 0.3 m^3/m^3 (Fig. 7(c)), the moisture profile at equilibrium is linear with depth (see Fig. 7(b)).

Table 2
Soil constitutive properties used for model simulation to evaluate errors in mass and energy balance

Properties	Values
Texture	3.9% sand, 65.1% silt, 31.0% clay
Porosity	0.46
Saturated hydraulic conductivity	4.74×10^{-7} m/s
Field capacity	0.294% by volume

3.3. Mass and energy balance

The LSP model is tested for the conservation of mass (moisture) and energy for a realistic scenario. The inputs to run the model including incoming radiant fluxes, air temperature, relative humidity, wind, and precipitation were obtained from our fourth radiobrightness energy balance experiment (REBEX-4) [23]. REBEX-4 was a collaborative experiment with the Climate Research Branch (CRB), Meteorological Service of Canada (MSC), Canada. It was conducted during the growing season from June 1996 through September, 1996 at the US Geological Survey's (USGS) Earth Resources Observation System (EROS) Data Center, about 30 km north-east of Sioux Falls, South Dakota, USA [15,16,23]. During the experiment, microwave brightnesses and micrometeorological parameters were observed for an artificially created bare soil site, and an undisturbed brome grass site concurrently. The bare soil site was monitored by CRB and was prepared by killing

the grass with a herbicide, and ploughing and disking the soil. The grass site was monitored by the UM-MGG.

The soil is modeled up to 5 m, with 9 nodes in the upper 5.5 cm and time-step for the simulation is 3 s. [1] The initial conditions for the upper 8 cm of soil moisture and temperatures are obtained from REBEX-4 observations. The initial temperature profile for the deeper layer is estimated from an annual model [30]. The moisture profile for the saturated layers below the water-table at 2 m is set equal to porosity. The profile is linearly interpolated for the soil blocks between 8 cm and 2 m. Soil constitutive properties are constant with depth as given in Table 2.

The LSP model required two modifications to make the model more relevant to the field conditions. The original version of the model had been calibrated only during drydown periods and did not include an infiltration model during precipitation events. The lower boundary condition did not allow for changes in heat and moisture content with time in the lowermost, nth, soil block, as mentioned in Section 2.1. To address the first limitation, a simple infiltration model was included to account for changes in infiltration with time and with soil properties. The maximum infiltration rate ($I_{\max}$), defined as the volume of water per unit area of soil that is allowed into the soil per second (m/s), depends on soil hydraulic and physical properties, soil temperature, vegetation cover, and surface characteristics like slope and roughness [14]. In the modified model, this $I_{\max}$ is estimated using a quasi-analytic solution to Richard's equation for vertical infiltration in a homogeneous soil with a constant initial moisture profile [17,36–38]. Such a solution (Eq. (8)) can be used because it is applied only to estimate $I_{\max}$ at the surface and the soil properties of the surface-block are homogeneous. The transport of moisture in the deeper nodes is governed by the conservation equations given in (1b).

$$i(t) = A + \frac{B}{2} t^{-\frac{1}{2}} \tag{8}$$

where,

$$A = \delta K_{\text{sat}}$$
$$B = 2K_{\text{sat}} \Psi_{\text{f}} (\theta_{\text{s}} - \theta_0)$$

where, δ is an empirical parameter set to 0.66 [37], K_{sat} is the saturated hydraulic conductivity, θ_{s} is the saturated moisture content, θ_0 is the moisture content before precipitation, and Ψ_{f} is the matric head of the wetting front estimated as the air entry pressure Ψ_0 [40].

The infiltration model included in the LSP model is physically simplistic in that it does not include the affect of ponded water on infiltration rate (I) when precipitation rate (P) is high. When P is less than the estimated I, the model uses P for moisture flux estimation at the surface, otherwise it uses I. Any excess rain during high P is treated as runoff.

To address the second limitation, the lower boundary conditions were altered, from conditions on energy and moisture fluxes to conditions on temperature and moisture content. Because the fluxes into and out of the nth soil block in the previous model were assumed equal, the heat and the moisture content did not change in the block over time. In the modified model, we set the temperature (T) and moisture (θ) at the nth block to be the same as those of the block above ($n-1$), i.e.,

$$\theta_{\text{m}}(n) = \theta_{\text{m}}(n-1) \quad T(n) = T(n-1) \tag{9}$$

This moisture condition implies that there is no capillary-driven force at the lower boundary. It is realistic because the lowermost soil block is at a depth of $\sim$5 m, which corresponds to saturated zones in the Great Plains region. The boundary condition for the temperature implies that there is no heat conduction at boundary. The zero temperature gradient condition is appropriate if the time required for a temperature change at the upper boundary to reach the lower boundary exceeds the duration of the simulation. A temperature change at the surface reaches the lower boundary at 5 m in approximately 73 days, based upon an analytical analysis similar to the one described in Section 3.1. To explore the behavior at 5 m, a temperature rise of 20 K was introduced at the surface of a 5 m soil column whose initial temperature and volumetric moisture were 293.15 K and 20%, respectively. The moisture was held at the equilibrium value and the lower boundary was closed to moisture or heat flow. Fig. 8 shows the temperature profile in the soil after 20, 50, 60, 73, and 80 days. There was a 0.001 K rise in temperature at the depth of 5 m after day 73. Applications of the model presented here are restricted to 20–30 days. If the simulations were inter-seasonal or annual, then we would need more sophisticated boundary conditions for the lower boundary.

After all the mass and energy fluxes at the upper and lower boundaries, and changes in the fluxes at all the nodes in the soil have been calculated, the following mass and energy balance should hold for the soil as a whole. For each time increment, δt,

$$q_{\text{m}}(0,1) - q_{\text{m}}(n,n+1) = \sum_{i=1}^{n} \delta (X_{\text{m}})_i \Delta z_i \tag{10a}$$

$$q_{\text{h}}(0,1) - q_{\text{h}}(n,n+1) = \sum_{i=1}^{n} \delta (X_{\text{h}})_i \Delta z_i \tag{10b}$$

where, Δz_i is thickness of the ith soil-block; $q_{\text{m}}(0,1)$ and $q_{\text{h}}(0,1)$ are the moisture and heat flux densities across the upper soil boundary, respectively; $q_{\text{m}}(n,n+1)$ and

[1] The conditions on time-step and number of nodes are obtained from convergence tests conducted with the REBEX-4 data and are described in [22].

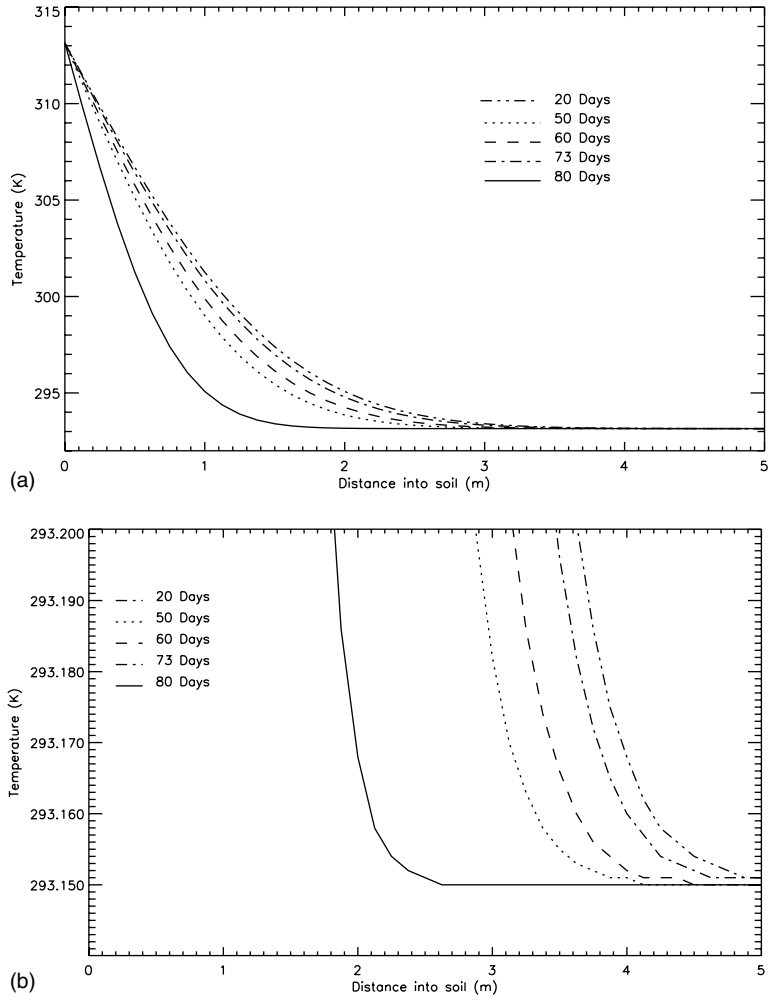

Fig. 8. Results from an analytic solution to calculate the time necessary for a thermal pulse at the surface to reach the lower boundary at the depth of 5 m. (a) Temperature profiles in soil as functions of time. (b) The temperature profiles zoomed-in to show the pulse at the surface reaching 5 m on the 73rd day.

$q_h(n, n+1)$, are the moisture and heat flux densities across the lower boundary, respectively; and $\delta(X_m)$, and $\delta(X_h)$ are the total moisture and heat content per unit volume, respectively.

Differences between the right and the left hand sides of Eqs. (10a) and (10b) represent the instantaneous errors in moisture balance (err_{mb}), and in energy balance (err_{eb}), respectively. The cumulative relative errors (CREs) for mass, err_{rm}, and for energy, err_{re}, are calculated with respect to the maximum of moisture and energy fluxes at the upper and the lower boundaries as shown in Eqs. (11a) and (11b), respectively. After a time interval, t_f,

$$\mathrm{err}_{rm} = \frac{\sum_{t=1}^{t_f} (\mathrm{err}_{mb})_t}{\sum_{t=1}^{t_f} \max[|q_m(0,1)|, |q_m(n,n+1)|]} \tag{11a}$$

$$\mathrm{err}_{re} = \frac{\sum_{t=1}^{t_f} (\mathrm{err}_{eb})_t}{\sum_{t=1}^{t_f} \max[|q_h(0,1)|, |q_h(n,n+1)|]} \tag{11b}$$

The CREs are used to evaluate accuracy of the numerical solution. Figs. 9 and 10 show these errors for a 12-day bare-soil model simulation during summertime, from Julian day 193 (June 11) through day 205 (June 23) in 1996. The CREs are negligible, relative to the magnitude of the incoming heat and moisture fluxes, throughout the simulation period (Figs. 9(a) and 10(a)). Figs. 9(b) and 10(b) present magnitude of instantaneous errors in mass and energy balance, respectively. The errors are very small, with the maximum error in moisture balance of 5×10^{-7} kg/m^2 and in energy balance of 2 J/m^2. The positive and negative CREs for mass and energy balance represent excess or deficit in total moisture and energy content in the modeled soil column, respectively. Fig. 9(c) shows the net moisture flux entering the upper boundary, with precipitation on Julian days 194, 196, 198, and 203. Fig. 10(c) shows the net incoming energy flux at the upper boundary which is primarily driven by insolation. Throughout the simulation period, energy fluxes vary slowly with time during

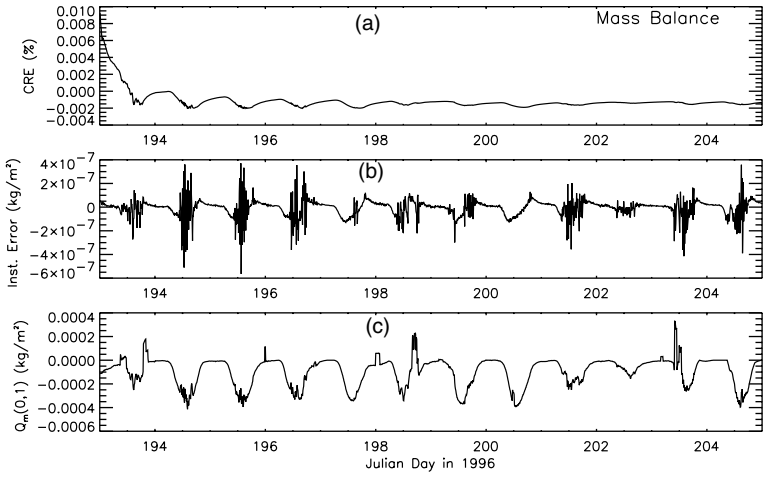

Fig. 9. Mass balance errors. (a) Cumulative relative errors as given by Eq. (11a). (b) Instantaneous error during each time step Δt. (c) Moisture flux incident on the upper boundary during each time step.

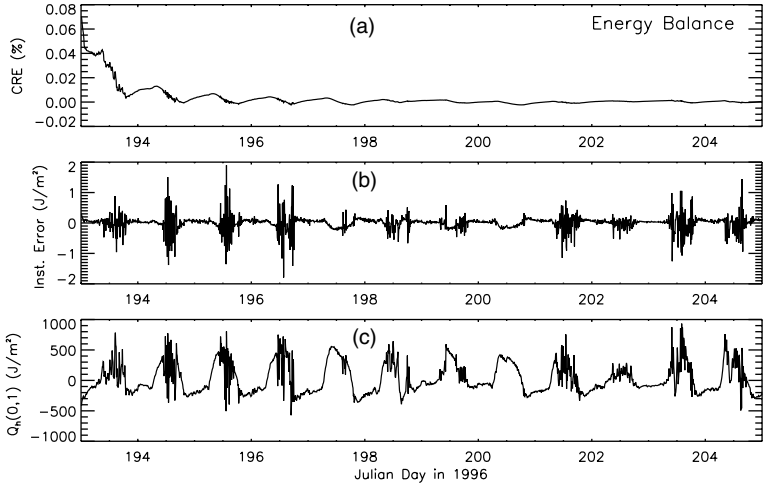

Fig. 10. Energy balance errors. (a) Cumulative relative errors as given by Eq. (11b). (b) Instantaneous error during each time step Δt. (c) Energy flux incident on the upper boundary during each time step.

the night and during clear days (Julian day 197 and 200), but change rapidly during partly cloudy days. Note that maximum errors coincide with the largest surface fluxes.

4. Summary

An LSP model, developed to be linked with a microwave emission model, was validated for its accuracy in implementation of the numerical methods. The numerical solution was compared with an analytic solution for strongly coupled moisture and energy transport in a vapor-dominated homogeneous soil. The two solutions compared well, with the maximum differences of 2.2 mK for temperature and $6 \times 10^{-4}\%$ for volumetric soil moisture. The model was tested for heat and moisture transport in a homogeneous soil with constant initial temperature and moisture profiles. The modeled energy propagated down the temperature gradient, and the moisture followed the negative of the temperature gradient and also followed gravity. The equilibrium profile for the soil moisture matched the slope of the soil-water retention curve. The LSP model was modified to extend for a realistic case and was shown to conserve mass and energy using inputs from field observations. The maximum errors in mass and energy were 5×10^{-7} kg/m^2 and 2 J/m^2, respectively, for a 12-day simulation period. These tests demonstrate the validity of the LSP model for the simple test-scenarios, and its extendibility to a more complex case.

Acknowledgements

The authors thank the anonymous reviewers for their helpful comments and suggestions to improve the

manuscript. Support for this research was provided by grants from the NASA Land Surface Hydrology Program.

Appendix A

A.1. Simplification of conservation equations

The conservation of mass and energy equations are simplified following [7] prior to applying the finite difference method to solve for temporal changes in soil temperature and moisture profiles.

A.1.1. Conservation of mass

$$\frac{\partial X_{\mathrm{m}}}{\partial t} = -\nabla \cdot \vec{q}_{\mathrm{m}} \tag{A.1}$$

$$X_{\mathrm{m}} = \rho_{\mathrm{l}}(\theta_{\mathrm{l}} + \theta_{\mathrm{v}}) \quad \vec{q}_{\mathrm{m}} = \vec{q}_{\mathrm{l}} + \vec{q}_{\mathrm{v}}$$
$$\frac{\partial(\theta_{\mathrm{l}} + \theta_{\mathrm{v}})}{\partial t} = -\frac{1}{\rho_{\mathrm{l}}} \nabla \cdot \vec{q}_{\mathrm{m}} \tag{A.2}$$

$$\frac{\vec{q}_{\mathrm{l}}}{\rho_{\mathrm{l}}} = -D_{\theta \mathrm{l}} - D_{T\mathrm{l}} \nabla T - K\hat{k} \quad \frac{\vec{q}_{\mathrm{v}}}{\rho_{\mathrm{l}}} = -D_{\theta \mathrm{v}} - D_{T\mathrm{v}} \nabla T$$
$$\frac{\vec{q}_{\mathrm{m}}}{\rho_{\mathrm{l}}} = -D_{\theta} - D_T \nabla T - K\hat{k} \tag{A.3}$$

$$\frac{\partial \theta_{\mathrm{l}}}{\partial t} = -\nabla \cdot \frac{\vec{q}_{\mathrm{l}}}{\rho_{\mathrm{l}}} - \mathbb{E} \quad \frac{\partial \theta_{\mathrm{v}}}{\partial t} = -\nabla \cdot \frac{\vec{q}_{\mathrm{v}}}{\rho_{\mathrm{l}}} + \mathbb{E} \tag{A.4}$$

where,

- X_{m} is the total moisture content per unit volume (kg/m^3),
- $\vec{q}_{\mathrm{l}}$, $\vec{q}_{\mathrm{v}}$, and $\vec{q}_{\mathrm{m}}$ are the liquid, vapor and moisture flux densities (kg/m^2 s), respectively,
- ρ_{l} is the density of liquid water (kg/m^3),
- θ_{l} and θ_{v} are the volumetric liquid water (m^3/m^3) and vapor content (m^3 of precipitable water/m^3), respectively, and $\theta = \theta_{\mathrm{l}} + \theta_{\mathrm{v}}$,
- T is the absolute temperature (K),
- D_T and D_θ are the thermal and isothermal moisture (liquid and vapor) diffusivities (m^2/K s), respectively,
- K is the unsaturated hydraulic conductivity (m/s), and
- $\mathbb{E}$ is the rate of evaporation (s^{-1}).

From Eq. (3) in [7], θ_{v} can be defined as

$$\theta_{\mathrm{v}} = (P - \theta_{\mathrm{l}}) \frac{\rho_0 h}{\rho_{\mathrm{l}}}$$

- P is the porosity m^3/m^3,
- ρ_0 is the density of saturated water vapor kg/m^3, and
- h is the relative humidity.

Taking the derivative of θ_{v} with respect to time, t,

$$\frac{\partial \theta_{\mathrm{v}}}{\partial t} = -\frac{\rho_{\mathrm{v}}}{\rho_{\mathrm{l}}} \left[\frac{\partial \theta_{\mathrm{l}}}{\partial t}\right] + \frac{P - \theta_{\mathrm{l}}}{\rho_{\mathrm{l}}} \left[h \frac{\partial \rho_0}{\partial t} + \rho_0 \frac{\partial h}{\partial t}\right]$$

$\rho_0 = f(T)$ and $h = f(T, \theta_{\mathrm{l}})$,

$$\frac{\partial \theta_{\mathrm{v}}}{\partial t} = \left[\frac{\rho_0(P - \theta_{\mathrm{l}})}{\rho_{\mathrm{l}}} \frac{\partial h}{\partial \theta_{\mathrm{l}}} - \frac{\rho_{\mathrm{v}}}{\rho_{\mathrm{l}}}\right] \frac{\partial \theta_{\mathrm{l}}}{\partial t} + \frac{P - \theta_{\mathrm{l}}}{\rho_{\mathrm{l}}} \left[h \frac{\partial \rho_0}{\partial T} + \rho_0 \frac{\partial h}{\partial T}\right] \frac{\partial T}{\partial t} \tag{A.5}$$

Inserting $\partial \theta_{\mathrm{v}}/\partial t$ from Eq. (A.5) in (A.2) and using $\vec{q}_{\mathrm{m}}/\rho_{\mathrm{l}}$ from Eq. (A.3),

$$\left\{1 + \frac{\rho_0(P - \theta_{\mathrm{l}})}{\rho_{\mathrm{l}}} \frac{\partial h}{\partial \theta_{\mathrm{l}}} - \frac{\rho_{\mathrm{v}}}{\rho_{\mathrm{l}}}\right\} \frac{\partial \theta_{\mathrm{l}}}{\partial t} + \frac{P - \theta_{\mathrm{l}}}{\rho_{\mathrm{l}}} \left\{h \frac{\partial \rho_0}{\partial T} + \rho_0 \frac{\partial h}{\partial T}\right\} \frac{\partial T}{\partial t} = \nabla \cdot \left[D_\theta \nabla \theta_{\mathrm{l}} + D_T \nabla T + K\hat{k}\right] \tag{A.6}$$

A.1.2. Conservation of energy

$$\frac{\partial X_{\mathrm{h}}}{\partial t} = -\nabla \cdot \vec{q}_{\mathrm{h}} \tag{A.7}$$

From Eqs. (10) and (11) in [7],

$$X_{\mathrm{h}} = C_{\mathrm{d}}(T - T_0) + L_0 \rho_{\mathrm{l}} \theta_{\mathrm{v}} + c_p \rho_{\mathrm{l}} \theta_{\mathrm{v}}(T - T_0) + c_{\mathrm{l}} \rho_{\mathrm{l}} \theta_{\mathrm{l}}(T - T_0) - \rho_{\mathrm{l}} \int_0^{\theta_{\mathrm{l}}} W \, \mathrm{d}\theta_{\mathrm{l}} \tag{A.8}$$

$$\vec{q}_{\mathrm{h}} = -\lambda \nabla T + L_0 \vec{q}_{\mathrm{v}} + c_p(T - T_0)\vec{q}_{\mathrm{v}} + c_{\mathrm{l}}(T - T_0)\vec{q}_{\mathrm{l}} \tag{A.9}$$

where,

- X_{h} is the total heat content per unit volume (J/m^3),
- $\vec{q}_{\mathrm{h}}$ is the heat flux density (J/m^2 s), respectively,
- C_{m} and C_{d} are the volumetric heat capacities of moist and dry soils (J/m^3 K), respectively,
- c_p and c_{l} are the specific heats (J/kg K) of water vapor at constant pressure and of liquid water, respectively,
- L_0 is the latent heat of vaporization (J/kg) at the reference temperature, T_0,
- W is the differential heat of wetting, and
- λ is the thermal conductivity of soil (J/m K s).

Taking the derivative of (A.8) with respect to time,

$$\frac{\partial X_{\mathrm{h}}}{\partial t} = C_{\mathrm{d}} \frac{\partial T}{\partial t} + \rho_{\mathrm{l}}\left[L_0 + c_p(T - T_0)\right] \frac{\partial \theta_{\mathrm{v}}}{\partial t} + c_{\mathrm{l}} \rho_{\mathrm{l}}(T - T_0) \frac{\partial \theta_{\mathrm{l}}}{\partial t} - \rho_l W \frac{\partial \theta_{\mathrm{l}}}{\partial t} \tag{A.10}$$

Taking the divergence of (A.9) and substituting $\nabla \cdot (\vec{q}_v/\rho_l)$ and $\nabla \cdot (\vec{q}_l/\rho_l)$ from (A.4),

$$\begin{aligned}-\nabla \cdot \vec{q}_h = {} & \lambda \nabla \cdot (\nabla T) - c_p \vec{q}_v \cdot \nabla T - c_l \vec{q}_l \cdot \nabla T \\ & + L_0 \rho_l \frac{\partial \theta_v}{\partial t} + c_p \rho_l (T - T_0) \frac{\partial \theta_v}{\partial t} \\ & + c_l \rho_l (T - T_0) \frac{\partial \theta_l}{\partial t} - L_0 \rho_l \mathbb{E} - c_p \rho_l (T - T_0) \mathbb{E} \\ & + c_l \rho_l (T - T_0) \mathbb{E} \end{aligned} \tag{A.11}$$

Equating (A.10) and (A.11)

$$\begin{aligned} C_d \frac{\partial T}{\partial t} - \rho_l W \frac{\partial \theta_l}{\partial t} = {} & \lambda \nabla \cdot (\nabla T) - c_p \vec{q}_v \cdot \nabla T \\ & - c_l \vec{q}_l \cdot \nabla T - L \rho_l \mathbb{E} \end{aligned} \tag{A.12}$$

Solving for $\mathbb{E}$ from Eqs. (A.3)–(A.5),

$$\begin{aligned} \mathbb{E} &= \frac{\partial \theta_v}{\partial t} + \frac{1}{\rho_l} \nabla \cdot \vec{q}_v \\ \mathbb{E} &= \left[\frac{\rho_0 (P - \theta_l)}{\rho_l} \frac{\partial h}{\partial \theta_l} - \frac{\rho_v}{\rho_l} \right] \frac{\partial \theta_l}{\partial t} \\ &\quad + \frac{P - \theta_l}{\rho_l} \left[h \frac{\partial \rho_0}{\partial T} + \rho_0 \frac{\partial h}{\partial T} \right] \frac{\partial T}{\partial t} - \nabla \cdot [D_{\theta_v} \nabla \theta_l + D_{T_v} \nabla T] \end{aligned} \tag{A.13}$$

Substituting $\mathbb{E}$ from (A.13), and $\vec{q}_v$ and $\vec{q}_l$ from (A.3) into (A.12),

$$\begin{aligned} & \left\{ L \rho_0 (P - \theta_l) \frac{\partial h}{\partial \theta_l} - L \rho_v - \rho_l W \right\} \frac{\partial \theta_l}{\partial t} \\ & \quad + \left\{ C_d - L (P - \theta_l) \left[h \frac{\partial \rho_0}{\partial T} + \rho_0 \frac{\partial h}{\partial T} \right] \right\} \frac{\partial T}{\partial t} \\ & = \nabla \cdot [(\lambda - L \rho_l D_{T_v}) \nabla T] + L \rho_l \nabla \cdot (D_{\theta_v} \nabla \theta_l) \\ & \quad + \rho_l \Big[(c_p D_{\theta_v} + c_l D_{\theta_l}) \nabla \theta_l \\ & \quad + (c_p D_{T_v} + c_l D_{T_l}) \nabla T + c_l K \hat{k} \Big] \cdot \nabla T \end{aligned} \tag{A.14}$$

Defining M and E as the coefficients from (A.6) and N and F from (A.14) for Eq. (4) in Section 2.2 as follows:

$$M = 1 + \frac{\rho_0 (P - \theta_l)}{\rho_l} \frac{\partial h}{\partial \theta_l} - \frac{\rho_v}{\rho_l} \tag{A.15}$$

$$E = \frac{P - \theta_l}{\rho_l} \left[h \frac{\partial \rho_0}{\partial T} + \rho_0 \frac{\partial h}{\partial T} \right] \tag{A.16}$$

$$N = L \rho_0 (P - \theta_l) \frac{\partial h}{\partial \theta_l} - L \rho_v - \rho_l W \tag{A.17}$$

$$F = C_d - L (P - \theta_l) \left[h \frac{\partial \rho_0}{\partial T} + \rho_0 \frac{\partial h}{\partial T} \right] \tag{A.18}$$

A.2. Analytic solution for Section 3.1

An analytic solution for the problem described in Section 3.1 follows Crank [6]. Eqs. (A.19a) and (A.19b) can be linearized in the form (A.19c) and (A.19d).

$$D \frac{\partial^2 \rho_v}{\partial z^2} - \frac{\partial}{\partial t} (\rho_v - \lambda_c T) = 0 \tag{A.19a}$$

$$\mathbb{D} \frac{\partial^2 T}{\partial z^2} - \frac{\partial}{\partial t} (T - v_c \rho_v) = 0 \tag{A.19b}$$

$$\Delta \rho_v = \rho_{v0} F_1 + f(F_1, F_2, \rho_{v0}, T_0) \tag{A.19c}$$

$$\Delta T = T_0 F_2 + f(F_1, F_2, \rho_{v0}, T_0) \tag{A.19d}$$

where D, $\mathbb{D}$, λ_c and v_c are constants that depend on soil properties [6],

- ρ_{v0} and T_0 are the initial changes in vapor density (kg/m^3) and temperature (K) forced at the upper boundary, respectively ($T_0 = 0$ for the problem in Section 3.1) and,
- $\Delta \rho_v$ and ΔT are the changes in vapor density and temperature profiles as functions of time.

The first terms on the right hand sides of the Eqs. (A.19c) and (A.19d) represent the solution if the diffusion of vapor density and temperature were de-coupled. The soil would come to an equilibrium with $\Delta \rho_v = \rho_{v0}$ and $\Delta T = T_0$, as functions F_1 and F_2 increased from $0 \to 1$ when time increased from $0 \to \infty$. The second terms represent the solution from coupling between the two diffusion processes.

The forms of F_1 and F_2 depend on the shape of the medium. The soil can be modeled as a plane sheet of thickness, n, and F_1 and F_2 become

$$\begin{aligned} F_1 = {} & \sum_{i=0}^{\infty} (-1)^i \operatorname{erfc} \frac{(2i+1)z - n}{2\sqrt{Dt}} \\ & + \sum_{i=0}^{\infty} (-1)^i \operatorname{erfc} \frac{(2i+1)z + n}{2\sqrt{Dt}} \end{aligned} \tag{A.20a}$$

$$\begin{aligned} F_2 = {} & \sum_{i=0}^{\infty} (-1)^i \operatorname{erfc} \frac{(2i+1)z - n}{2\sqrt{\mathbb{D}t}} \\ & + \sum_{i=0}^{\infty} (-1)^i \operatorname{erfc} \frac{(2i+1)z + n}{2\sqrt{\mathbb{D}t}} \end{aligned} \tag{A.20b}$$

where

- $\operatorname{erfc} x = 1 - (2/\pi^{1/2}) \int_0^x \exp(-\eta^2)\, d\eta$,
- z is the depth in soil (m) and,
- t is the time (s).

The change in temperature, ΔT, vapor density, $\Delta \rho_v$, and moisture, ΔV_f, as functions of depth and time are given by Crank [6] as follows:

$$\Delta T = T_0 F_2 - \frac{(1-\mu_2^2\mathbb{D})T_0 - v_c\rho_{v0}}{\mathbb{D}(\mu_1^2-\mu_2^2)}(F_2-F_1) \quad \text{(A.21a)}$$

$$\Delta\rho_v = \rho_{v0}F_1 - \frac{(1-\mu_1^2 D)\rho_{v0} - \lambda_c T_0}{D(\mu_1^2-\mu_2^2)}(F_2-F_1) \quad \text{(A.21b)}$$

$$\Delta V_f = \sigma_c\Delta\rho_v - \omega_c\Delta T \quad \text{(A.21c)}$$

where,

$$\mu_1^2 = \frac{1}{D} + \frac{\lambda_c v_c}{\mathbb{D}-D} \quad \mu_2^2 = \frac{1}{\mathbb{D}} - \frac{\lambda_c v_c}{\mathbb{D}-D}$$
$$\sigma_c = \frac{\partial V_f}{\partial\rho_v} \quad \omega_c = \frac{\partial V_f}{\partial T}$$

The Eq. (1a) can be linearized to match the form of Eqs. (A.19a) and (A.19b) if we assume negligible transport of sensible heat by water vapor and negligible liquid flow, as follows [34]:

$$\theta_a\frac{\partial\rho_v}{\partial t} + (\rho_l-\rho_v)\frac{\partial\theta_m}{\partial t} = \frac{\partial}{\partial z}\left[D_m\frac{\partial\rho_v}{\partial z}\right] \quad \text{(A.22a)}$$

$$C_m\frac{\partial T}{\partial t} - \rho_l(L+W)\frac{\partial\theta_m}{\partial t} = \frac{\partial}{\partial z}\left[\left(\lambda - D_m\frac{\partial\rho_v}{\partial T}\bigg|_\Psi\right)\frac{\partial T}{\partial z}\right] \quad \text{(A.22b)}$$

where,

$$L = L_0 + (c_p - c_l)(T - T0)$$

- θ_a, ρ_v, ρ_l, λ, C_m, c_l, c_p, L_0, T, T_0 and W have been defined for Eq. (1b),
- θ_m is the volumetric moisture content (m^3/m^3),
- D_m is an effective molecular diffusivity (m^2/s) and,
- Ψ is the matric head (m).

References

[1] Beljaars A, Viterbo P, Miller M, Betts A. The anomalous rainfall over the US during July 1993—sensitivity to land-surface parametrization and soil moisture. Month Weat Rev 1996;124(3):362–83.

[2] Bonan G. A Land Surface Model (LSM Version 1.0) for ecological, hydrological, and atmospheric studies: Technical description and user's guide. Tech. Rep. NCAR/TN-417+STR, Climate and Global Dynamics Division, NCAR, January 1996.

[3] Burke E, Shuttleworth W, Lee K, Bastidas L. Using area-average remotely sensed surface soil moisture in multipatch land data assimilation systems. IEEE Trans Geosci Remote Sensing 2001;39(10):2091–100.

[4] Cahill A, Parlange M. On water vapor transport in field soils. Water Resour Res 1998;34(4):731–9.

[5] Camillo P, Gurney R, Schmugge T. A soil and atmosphere boundary layer model for evapotranspiration and soil moisture studies. Water Resour Res 1983;19(2):371–80.

[6] Crank J. The mathematics of diffusion. Oxford: Clarendon Press; 1975.

[7] de Vries D. Simultaneous transfer of heat and moisture in porous media. Trans Am Geophys Union 1958;39(5):909–16.

[8] de Vries D. Thermal properties of soils. In: Physics of Plant Environment. New York: Interscience Publishers; 1963. p. 210–35.

[9] Dickinson R, Henderson-Sellers A, Kennedy P. Biosphere–atmosphere transfer scheme (BATS) version 1e as coupled to the NCAR Community Climate Model. Tech. Rep. NCAR/TN-387+STR, Climate and Global Dynamics Division, NCAR, August 1993.

[10] Dickinson R, Henderson-Sellers A, Kennedy P, Wilson M. Biosphere–atmosphere transfer scheme (BATS) for the NCAR Community Climate Model. Tech. Rep. NCAR/TN-275+STP, Atmospheric Analysis and Prediction Division, NCAR, December 1986.

[11] Entekhabi D, Nakamura H, Njoku E. Solving the inverse problem for soil moisture and temperature profiles by sequential assimilation of multifrequency remotely sensed observations. IEEE Trans Geosci Remote Sensing 1994;32(2):438–48.

[12] Galantowicz J, England A. Seasonal snowpack radiobrightness interpretation using a SVAT-linked emission model. J Geophys Res 1997;102(D18):21933–46.

[13] Galantowicz J, Entekhabi D, Njoku E. Tests of sequential data assimilation for retrieving profile soil moisture and temperature from observed 1 band radiobrightness. IEEE Trans Geosci Remote Sensing 1999;37(4):1860–70.

[14] Ghildyal B, Tripathi R. Soil physics. New York: John Wiley; 1987.

[15] Goodison B, Metcalfe J, McNichol D, Davey M, Le, H. Participation in REBEX-4: data collection and completion phase report. Tech. rep., Atmospheric Environment Service, Canada, 1996.

[16] Goodison B, Metcalfe J, McNichol D, Davey M, Le H. Participation in REBEX-4: installation phase report. Tech. rep., Atmospheric Environment Service, Canada, 1996.

[17] Green W, Ampt G. Studies on soil physics. J Agri Sci 1911; 4(5):1.

[18] Haverkamp R, Vauclin M, Tauma J, Wierenga P, Vachaud G. A comparison of numerical simulation models for one-dimensional infiltration. Soil Sci Soc Am J 1977;41(2):285–94.

[19] Houser P, Shuttleworth W, Famiglietti J, Gupta H, Syed K, Goodrich D. Integration of soil moisture remote sensing and hydrologic modeling using data assimilation. Water Resour Res 1998;34(12):3405–20.

[20] Jackson T, O'Neill P. Temporal observations of surface soil moisture using a passive microwave sensor. Remote Sens Environ 1987;21:281–96.

[21] Jackson T, Schmugge T, O'Neill P. Passive microwave remote sensing of soil moisture from an aircraft platform. Remote Sens Environ 1984;14:135–42.

[22] Judge J. Land surface process and radiobrightness modeling of the great plains. Ph.D. thesis, University of Michigan, 1999.

[23] Judge J, England A. Field data report for the fourth radiobrightness energy balance experiment (REBEX-4): June–September 1996. Tech. Rep. Rad. Lab. Tech. Note RL-974, University of Michigan, 1999.

[24] Kim E. Remote sensing of land surface conditions in arctic tundra regions for climatological applications using microwave radiometry. Ph.D. thesis, University of Michigan, 1999.

[25] Kimball B, Jackson R, Reginato R, Nakayama F, Idso S. Comparison of field-measured and calculated soil-heat fluxes. Soil Sci Soc Am J 1976;40:18–25.

[26] Lai S, Tiedje J, Erickson A. In situ measurement of gas diffusion coefficients in soils. Soil Sci Soc Am Proc 1976;40:3–6.

[27] Lakshmi V. A simple surface temperature assimilation scheme for use in land surface models. Water Resour Res 2000;36(12):3687–700.

[28] Liang X, Lettenmaier D, Wood E, Burges S. A simple hydrologically based model of land surface water and energy fluxes for general circulation models. J Geophys Res 1994;99(D7):14415–28.
[29] Liang X, Lettenmaier D, Wood E, Burges S. One-dimensional stastical dynamical representation subgrid spatial variability of precipitation in the 2-layer variable infiltration capacity model. J Geophys Res 1996;101(D16):21403–22.
[30] Liou Y, England A. Annual temperature and radiobrightness signatures for bare soils. IEEE Trans Geosci Remote Sensing 1996;34(4):981–90.
[31] Liou Y, England A. A land surface process/radiobrightness model with coupled heat and moisture transport in soil. IEEE Trans Geosci Remote Sensing 1998;36(1):273–86.
[32] Liou Y, England A. A land surface process/radiobrightness model with coupled heat and moisture transport for freezing soils. IEEE Trans Geosci Remote Sensing 1998;36(2):669–77.
[33] Liou Y, Galantowicz J, England A. A land surface process/radiobrightness model with coupled heat and moisture transport for prairie grassland. IEEE Trans Geosci Remote Sensing 1999;37(4):1848–59.
[34] Milly P. Moisture and heat transport in hysteretic, inhomogeneous porus media: A matric head-based formulation and a numerical method. Water Resour Res 1982;18(3):489–98.
[35] Noilhan J, Planton S. A simple parametrization of land surface processes for meterological models. Month Weat Rev 1989; 117(March):536–49.
[36] Philip J. Theory of infiltration, 1. The infiltration equation and its solution. Soil Sci 1957;83(5):345–57.
[37] Philip J. Inverse solution for one-dimensional infiltration and ratio A/K1. Water Resour Res 1987;26(9):2023–7.
[38] Philip J. The infiltration joining problem. Water Resour Res 1987;23(12):2239–45.
[39] Philip J, deVries D. Moisture movement in porous materials under temperature gradients. Tmns Am Geophys Union 1957; 38(2):222–32.
[40] Reible D, Illangasekare T, Doshi D, Malhiet M. Infiltration of immiscible contaminants in unsaturated zone. Ground Water 1990;28(5):685–92.
[41] Reichle RH, Entekhabi D, McLaughlin D. Downscaling of radiobrightness measurements for soil moisture estimation: a four-dimensional variational data assimilation approach. Water Resour Res 2001;37(9):2353–64.
[42] Reichle R, McLaughlin D, Entekhabi D. Variational data assimilation of microwave radiobrightness observations for land surface hydrologic applications. IEEE Trans Geosci Remote Sensing 2001;39(8):1708–18.
[43] Rossi C, Nimmo J. Modeling of soil water retention from saturation to oven dryness. Water Resour Res 1994;30(3):701–8.
[44] Schmugge T, Jackson T. A dielectric model of the vegetation effects on the microwave emission from soils. IEEE Trans Geosci Remote Sensing 1992;30(4):757–60.
[45] Sellers P, Mintz Y, Sud Y, Dalcher A. A simple biosphere model SiB for use within general circulation models. J Atmos Sci 1986;43(6):505–31.
[46] Trenberth KE. Climate system modeling. New York: Cambridge University Press; 1995.
[47] Verseghy SB, McFarlane N, Lazare M. CLASS-A Canadian land suface scheme for GCMs. ii. vegetation model and coupled runs. Int J Climatology 1993;13:347–70.
[48] Walker J, Houser P. A methodology for initializing soil moisture in a global climate model: assimilation of near-surface soil moisture observations. J Geophys Res 2001;106(D11):11761–74.
[49] Xue Y, Sellers P, Kinter J, Shukla J. A simplified biosphere model for global climate studies. J Clim 1991;4(March):345–64.